Revision 2

Crystal structure of calcium-ferrite type $NaAlSiO_4$ up to 45 GPa

Fei Qin[1,5*], Ye Wu[2], Shengchao Xue[1], Dongzhou Zhang[3], Xiang Wu[4], Steven D. Jacobsen[5]

[1]*School of Earth Sciences and Resources, China University of Geosciences (Beijing), Beijing, China*

[2]*School of Science, Wuhan University of Technology, Wuhan, China*

[3]*School of Ocean and Earth Science and Technology, Hawai'i Institute of Geophysics and Planetology, University of Hawaii at Manoa, Honolulu, Hawaii, USA*

[4]*State Key Laboratory of Geological Processes and Mineral Resources, China University of Geosciences, Wuhan, China*

[5]*Department of Earth and Planetary Sciences, Northwestern University, Evanston, Illinois, USA*

Corresponding author: Fei Qin

Email: fei.qin@cugb.edu.cn

Abstract

Alkali-rich aluminous high-pressure phases including calcium-ferrite (CF) type $NaAlSiO_4$ are thought to constitute ~20% by volume of subducted mid-ocean ridge basalt (MORB) under lower mantle conditions. As a potentially significant host for incompatible elements in the deep mantle, knowledge of the crystal structure and physical properties of CF-type phases is therefore important to understanding the crystal chemistry of alkali storage and recycling in the Earth's mantle. We determined the evolution of the crystal structure of pure CF-$NaAlSiO_4$ and Fe-bearing CF-$NaAlSiO_4$ at pressures up to ~45 GPa using synchrotron-based, single-crystal X-ray diffraction. Using the high-pressure lattice parameters, we also determined a third-order Birch-Murnaghan equation of state, with V_0 = 241.6(1) Å^3, K_{T0} = 220(4) GPa and K_{T0}' = 2.6(3) for Fe-free CF, and V_0 = 244.2(2) Å^3, K_{T0} = 211(6) GPa and K_{T0}' = 2.6(3) for Fe-bearing CF. The addition of Fe into CF-$NaAlSiO_4$ resulted in a 10±5% decrease in the stiffest direction of linear compressibility along the *c*-axis, leading to stronger elastic anisotropy compared with the Fe-free CF phase. The NaO_8 polyhedra volume is 2.6 times larger and about 60% more compressible than the octahedral (Al,Si)O_6 sites, with $K_0^{NaO_8}$ = 127 GPa and $K_0^{(Al,Si)O_6}$ ~304 GPa. Raman spectra of the pure CF-type $NaAlSiO_4$ sample shows that the pressure coefficient of the mean vibrational mode, 1.60(7) cm^{-1}/GPa, is slightly higher than 1.36(6) cm^{-1}/GPa obtained for the Fe-bearing CF-$NaAlSiO_4$ sample. The ability of CF-type phases to contain incompatible elements such as Na beyond the stability field of jadeite requires larger and less compressible NaO_8 polyhedra. Detailed high-pressure crystallographic

information for the CF phases provides knowledge on how large alkali metals are hosted in alumina framework structures with stability well into the lowermost mantle.

Keywords: CF-type $NaAlSiO_4$, single-crystal structure refinements, incompatible Na elements, high pressures, Raman spectroscopy, lower mantle

Introduction

The bulk lower mantle is considered well mixed above the D'' layer, yet regional heterogeneities are identified by seismology and geochemical studies (e.g. Jenkins et al., 2017; Romanowicz and Wenk, 2017). Calcium-ferrite (CF) type phases and the new hexagonal aluminous phase (NAL phase) may collectively account for 10-30 vol% of subducted oceanic crust below ~2700 km and therefore likely play an important role in the observed regional-scale seismological and geochemical heterogeneities (Bina and Helffrich, 2014; French and Romanowicz, 2014; Fukao et al., 2009; Litasov and Ohtani, 2005; Wu et al., 2016, 2017). However, the high-pressure behaviors (e.g., structure, stability and elasticity) of the alkali-rich aluminous high-pressure phases remains poorly known compared with other lower mantle minerals such as bridgmanite $(Mg,Fe)SiO_3$), davemaoite ($CaSiO_3$), and ferropericlase (Mg,Fe)O) (Fujino et al., 2012; Ono et al., 2004; Wentzcovitch et al., 1995). Determining the structure and thermodynamic properties of the major alkali-rich phases will therefore improve computational models of slab dynamics as well as our understanding of the behavior of incompatible elements in the lowermost mantle.

Average mid-ocean ridge basalt contains 10-12 wt.% CaO and 2-3 wt.% Na_2O, largely in plagioclase and clinopyroxenes in the upper mantle (Sun et al., 1979). On subduction to below 50-60 km, the basalt-eclogite transition changes the mineralogy of MORB where Ca-pyroxene (diopside), Na-pyroxene (jadeite) and garnet host the majority of alkali metals and aluminum (Yoder Jr and Tilley, 1962; Ringwood and Green, 1966). Below ~300 km, pyroxene and garnet form a solution of majoritic

garnet but below the transition zone (410-660 km) the breakdown of majoritic garnet leads to bridgmanite, davemaoite, and stishovite, where Al, the majority of Na, and some Ca are hosted in the CF-type and/or NAL-phases (depending on depth) with complex chemical composition (Kesson et al., 1994; Ono et al., 2001; Ricolleau et al., 2010).

CF phases crystallizing in the orthorhombic system (space group *Pbnm*) display solid solutions with the general formula $A_3B_6O_{12}$, where A represents a large mono- or divalent cations, like Na^+, K^+, or Ca^{2+}, and B is a six-coordinated cation site occupied by Mg^{2+} and mixed-valence Fe. Incorporation of Al^{3+} or Si^{4+} into the octahedral site leads to CF-type phases $CaAl_2O_4$, $MgAl_2O_4$, and $NaAlSiO_4$ (Irifune et al., 1991; Liu, 1977; Reid and Ringwood, 1969). Along the $NaAlSiO_4$-$MgAl_2O_4$ join, NAL is formed as a single phase up to 34 GPa, whereas above 45 GPa, $NaAlSiO_4$ and $MgAl_2O_4$ co-exist as separate phases in the calcium-ferrite structure (Imada et al., 2011). Given that these likely exist as separate phases over most of the depth range in lower mantle, experimental determination of their physical properties is needed to properly estimate the density and velocity of subducted slabs (Ricolleau et al., 2010). Furthermore, by examining the influence of iron incorporation it is also possible to evaluate potential impacts of iron spin-pairing transitions (e.g. Lobanov et al., 2017; Wu et al., 2017).

To gain insight into the elasticity and equations of state as well as alkali storage mechanisms, we have undertaken high-precision, single-crystal structure determinations of Fe-free and Fe-bearing CF phases up to ~45 GPa *in situ* using synchrotron-based single-crystal X-ray diffraction. Vibrational properties of these

97 structures were determined by Raman spectroscopy. These results provide
98 comprehensive understanding of the crystallographic information of such alkali-
99 bearing CF phases under lower mantle conditions, thus improving our knowledge of
100 proper chemical and physical properties of these important lower mantle alkali-
101 dominated phases, and shedding new light on alkali reservoirs in the Earth's deep
102 mantle.
103
104 **Materials and methods**

105 Samples for the current study were synthesized in experimental runs #5K2124
106 (Fe-free) and #5K2681 (Fe-bearing) at 25 GPa and 1600 °C using a 5000-ton Kawai-
107 type multi anvil pressure apparatus (USSA-5000) at the Institute for Study of the
108 Earth's Interior (ISEI), Okayama University at Misasa, Japan. Details of the sample
109 synthesis and compositional characterization are reported in Wu et al. (2017). Briefly,
110 a stoichiometric mixture of high-purity Na_2CO_3, Al_2O_3, and SiO_2 were mixed with a
111 molar ratio of 1:1:2 and used as the starting material. For the Fe-bearing sample, iron
112 was added as $^{57}Fe_2O_3$ with >95% enrichment in ^{57}Fe. The chemical compositions of
113 the Fe-free and Fe-bearing samples were obtained by electron microprobe analysis as
114 given by Wu et al. (2017) and found to be $Na_{0.93}Al_{1.02}Si_{1.00}O_4$ and
115 $Na_{0.88}Al_{0.99}Fe_{0.13}Si_{0.94}O_4$. Their crystal structure was characterized by X-ray
116 diffraction at GSECARS of the Advanced Photon Source (APS), Argonne National
117 Laboratory, beamline 13-BM-C. The results confirm that both CF samples possess
118 space group *Pbnm*, and their lattice constants are a = 10.166(1) Å, b = 8.675(9) Å, c =

119 2.7380(6) Å, and V = 241.5(1) Å^3 for the Fe-free CF phase, and a = 10.189(2) Å, b =
120 8.686(7) Å, c = 2.7571(4) Å, and V = 244.0(2) Å^3 for the Fe-bearing sample.
121 Mössbauer spectroscopy shows that 90% of the iron is ferric (Fe^{3+}) (Wu et al., 2017).
122 Crystals of the CF phases measuring ~1.5 mm in maximum dimension were crushed
123 into 30 μm × 40 μm chips under an optical microscope and then polished to ~10 μm
124 thickness for the high-pressure study.

125 High-pressure, single-crystal X-ray diffraction experiments were carried out at
126 GSECARS (Sector 13) of the advanced Photon Source (APS), Argonne National
127 Laboratory (ANL), beamline 13-BM-C. A monochromatic X-ray beam with a
128 wavelength of 0.434 Å was focused to a 15×15 μm^2 spot for the diamond-anvil cell
129 experiment (Zhang et al., 2017). We used a short symmetric-type diamond anvil cells,
130 fitted with Boehler-Almax diamond anvils with 300 μm flat culets and set into seats
131 with 76-degree opening. A Re gasket was pre-indented to ~40 μm thickness before
132 laser drilling a sample chamber of ~160 μm diameter. Polished Fe-free and Fe-bearing
133 CF samples were loaded with neon pressure medium into their respective sample
134 chambers along with Pt foil for pressure calibration (Fei et al., 2007).

135 To obtain sufficiently precise constraints on the unit-cell evolution, we obtained
136 diffraction data with multiple detector positions and for the full structure
137 determinations at least 600 reflections were used (Figure S1). The single-crystal
138 crystal structure refinements of the CF samples were carried out using ATREX/RSV,
139 SHELXL, Olex2 and VESTA software packages (Dera et al., 2013; Dolomanov et al.,
140 2009; Momma and Izumi, 2008). A crystal structure model of Yamada et al. (1983)

was used to initialize the refinement. We used isotropic atomic displacement parameters (U_{iso}) for all atoms. Figures of merits of the refinements, atomic coordinates and displacement parameters of Fe-free CF phase is presented in Supplemental information Table S1 and S2.

High-pressure Raman spectroscopy for the iron-bearing and pure CF-$NaAlSiO_4$ phases was performed up to 44.6 GPa at room temperature using Princeton-style diamond-cells with 300-μm ultra-low fluorescent diamond anvils. The diamond cells for Raman spectroscopy were gas loaded with neon at HPSTAR and ruby was used as the pressure calibration (Mao et al., 1986). The pressure was determined by multiple measurements before and after each experimental run. Raman spectra were collected on a Renishaw inVia reflex Raman spectrometer with 532 nm diode-pumped solid-state laser, at Peking University. The spectrograph was calibrated using a silicon wafer, and the spectra were collected in unpolarized, backscatter geometry using a charge-coupled device detector with a resolution of 1 cm^{-1}. Each Raman spectrum was collected with an averaged exposure time of 30 s over 5 accumulations. The deconvolution of Raman spectra and peak positions were fitted using the software package PeakFit (Systat Software, Inc.)

Results and Discussion

Stability and compressibility of Fe-free and Fe-bearing CF phase

Throughout the investigated pressure range (up to 41.3 and 44 GPa for Fe-free

and Fe-bearing CF, respectively), no indicators of phase transformation were identified. The crystal structure of Fe-free CF-$NaAlSiO_4$ at 41.3 GPa is shown in Figure 1. The CF phase consists of an alumina framework composed of double chains of linked $(Al,Si)_1O_6$- and $(Al,Si)_2O_6$-octahedra, while relativity large alkali Na sites located in the eight-fold coordination sites in tunnels formed by the octahedral chains, hereafter denoted NaO_8-polyhedra. The quality of diffraction patterns used to carry out structure refinements at low (~2 GPa) and high (~40 GPa) pressures are illustrated by the CCD images shown in Figure S1.

Lattice parameters of the CF phase are consistently refined to an orthorhombic cell (*Pbnm* and $Z = 4$) (Figure 2). Volume compression and axial compression data of both CF phases at different pressures are given in Table S3 and S4. Pressure-volume data were fitted to a third-order Birch-Murnaghan equation of state (EoS) using error-weighted least squares with EoSFit7c software (Angel et al., 2014). Under ambient conditions, the measured V_0 values are 241.5(1) and 244.0(2) $Å^3$ for the Fe-free and Fe-bearing CF sample, respectively. The best-fit, third-order Birch-Murnaghan EoS parameters yield $V_0 = 241.6(1)$ $Å^3$, $K_{T0} = 220(4)$ GPa and $K_{T0}' = 2.6(3)$ for Fe-free CF, and $V_0 = 244.2(2)$ $Å^3$, $K_{T0} = 211(6)$ GPa with $K_{T0}' = 2.6(3)$ for Fe-bearing CF. Note that at room pressure, the measured unit-cell volume and the fitted zero-pressure volume in our BM3 procedure are identical within error for both Fe-free and Fe-bearing phases. Although both CF phases exhibit broadly similar equation of state parameters, the unit-cell volume of the Fe-bearing sample is about 1% larger and about 4% more compressible than the Fe-free sample.

We also determined the axial compressibility of the lattice parameters using the linearized third-order Birch-Murnaghan EoS (Figure 2). Details are described in Supplemental Text S1. Our fitted linear moduli to *a*, *b* and *c* axes are 158(5), 180(8) and 338(9) GPa for Fe-free CF phase, and 158(11), 181(7) and 306(16) GPa for Fe-bearing CF sample, respectively, which indicate *a*- and *b*-axes exhibit similar linear moduli for both CF phases. The addition of Fe into the CF phase leads to a decrease in the linear compressibility of the *c*-axis compared with Fe-free phase. The relative axial compressibility scheme is $\beta_a > \beta_b > \beta_c$ for both phases. Ratios of zero-pressure axial compressibility between the three axes are 2.14:1.88:1 for Fe-free and 1.94:1.69:1 for Fe-bearing sample, which suggests strong elastic anisotropy on compression, with the *c*-axis being the stiffest direction within the structure.

The room temperature equations of state for CF phases determined in this study are shown in Figure 3, with volume normalized to measured V_0 in order to aid in comparison with previous studies. The absolute difference between our equation of state parameters and those from previous work (Table S5 in supporting information) depends on many factors including (among others) data precision, data density, crystal quality, and the experimental pressure range, resulting in the usual trade-offs between V_0, K_{T0}, and K'_{T0} fitted to different datasets, complicating a quantitative assessment of the effect of Fe substitution on the compressibility of CF phase. By measuring both pure-CF and Fe-bearing CF phases in the same study with high-quality single crystals, we were able to tightly constrain the values of K_{T0} and K'_{T0} for both crystals under similar experimental parameters, finding that Fe_{tot} = 0.13 pfu in the CF phase leads to

206 3.2±1.9% reduction in the bulk modulus compared with the Fe-free sample. The lower
207 bulk moduli values of K_{T0} = 201(9) GPa reported for the CF-phase by Wu et al.
208 (2017), who also determined high-spin (K_{T0} = 208(3) GPa) and low-spin (K_{T0} = 202(7)
209 GPa) bulk moduli for Fe-bearing CF phase were fitted with relatively high values of
210 K'_{T0} (fixed at 4), which are, however, poorly constrained. The derived EoS parameters
211 obtained in this study are statistically higher than that obtained by Guignot and
212 Andrault (2004) with K_{T0} = 185(5) GPa but in good agreement with previously
213 reported values of K_{T0} = 214(14) GPa, K_{T0}' = 3.6(5) (Imada et al., 2012) and K_{T0} =
214 220(1) GPa, K_{T0}' = 4.1(1) (Dubrovinsky et al., 2002).

215 Generally, CF phases in MORB compositions exhibit complex solid solutions
216 but for simplicity can be considered along the $NaAlSiO_4$-$MgAl_2O_4$ join (Imada et al.,
217 2011). By comparison, solid solutions between $NaAlSiO_4$ and $MgAl_2O_4$ in the
218 $CaFe_2O_4$ structure type show roughly similar density between these two end members.
219 However, there is a very broad range of reported values for the bulk modulus of the
220 $CaFe_2O_4$-type $MgAl_2O_4$ phase in MORB composition, ranging from 184–243 GPa
221 (Funamori et al., 1998; Irifune et al., 2002; Guignot and Andrault, 2004; Ono et al.,
222 2005). The thermal equation of state of $MgAl_2O_4$ has also been investigated using
223 multi-anvil apparatus and DAC techniques by Sueda et al. (2009), who reported 205(6)
224 GPa for the room-temperature bulk modulus.

225

226 **High-pressure structure evolution of CF phase**

227 To better understand the compression mechanisms of CF-type $NaAlSiO_4$, we

analyzed the structure and evolution of the polyhedral elements on compression at selected pressures. Here we used two parameters to characterize the compression of each polyhedron: the polyhedral volume and the mean bond length. Results are given in Table S6. More details on the high-pressure structure refinements of the Fe-free sample will be discussed next.

The bond lengths of Na-O, (Al,Si)1–O and (Al,Si)2–O as a function of pressure are shown in Figure 4. Average (Al,Si)–O distances related to the (Al,Si)1 and (Al,Si)2 sites are 1.856 Å and 1.876 Å at room pressure, respectively. By comparing with those aluminous high-pressure phases, these values are in good agreement with 1.929 Å in $NaAlSi_2O_6$ jadeite (Cameron et al., 1973) and 1.887 Å in $Mg_3Al_2Si_3O_{12}$ pyrope (Novak and Gibbs, 1971), which are typical values for the six-coordinated Al–O distances. During static compression, all of the bond distances decrease linearly in the range of 0.00168-0.00172 Å/GPa for (Al,Si)–O bond, while the shortening of Na–O bonds are about twice than that of the (Al,Si)–site octahedral bonds. Over the whole pressure range of this study, the mean bond length of Na–O shortened by 6.7%, whereas the (Al,Si)–O bonds shortened by only 3.6% for (Al,Si)1–O and 3.7% for (Al,Si)2–O.

The structural evolution of all the coordination polyhedra is presented in Figure 5. The average $(Al,Si)O_6$ volume is 8.48(2) $Å^3$ at ambient pressure and decreases to 7.62(2) $Å^3$ at 41.0 GPa, while the volume of NaO_8-polyhedron is about 2.6 times larger, and decreases from 22.40(3) $Å^3$ to 18.37(2) $Å^3$ between 0 and 41.0 GPa. The average $(Al,Si)O_6$ volume has a much smaller value and is significantly more

incompressible than the NaO_8-polyhedron. In particular, the $(Al,Si)O_6$ octahedron is much stiffer with an average bulk modulus of ~304 GPa compared with the $K_0^{NaO_8}$ of 127 GPa within the whole pressure range, when both K_0' fixed at 4. Our value of $K_0^{SiO_6}$ for CF phase is in excellent agreement with the compressibility of SiO_6 octahedron in stishovite SiO_2 ($K_0^{SiO_6}$ = 303-346 GPa), another important phase in the lower mantle (Andrault et al., 1998).

The distortion index (D) describes the polyhedral distortion, defined as $D = \frac{1}{n}\sum_{i=1}^{n}\frac{|l_i - l_{av}|}{l_{av}}$, where l_i is the distance from the central cation to the i_{th} surrounding oxygen and l_{av} is the average distance (Baur, 1974; Momma and Izumi, 2008). In this study, we found that NaO_8 polyhedra have higher distortion indices than the $(Al,Si)O_6$ octahedra across the experimental pressure range. At 41 GPa, D_{NaO8} is 0.029 while the average $D_{(Al,Si)O6}$ is 0.0078. Distortion index values of the NaO_8 did not change beyond error during compression, indicating that the NaO_8 polyhedra have less structural deformation compared with the $(Al,Si)O_6$ upon compression (Figure 6).

Vibrational modes and Grüneisen parameters

In situ Raman spectroscopy was conducted up to 44.6 GPa on both Fe-free and Fe-bearing crystals taken from the same synthesis runs used in the XRD study. Selected spectra of both crystals with increasing pressure are presented in Figure 7. As the Raman active modes are $18A_g+9B_{1g}+18B_{2g}+9B_{3g}$, a total of 54 Raman active vibrations modes are expected. Unfortunately, the data quality is not rich enough to deconvolute and assign all the peaks. The smaller number of observed modes is due to

weak intensity, peak overlap, and orientation dependence. In this study, around 14 Raman peaks were observed for the CF in the Raman shift range of 1200-150 cm^{-1}. Peak positions of the major observed modes as a function of pressure are provided in Figure 7 and Table S7. All observed Raman peaks shift to higher frequency with increasing pressure, and some broad bands may consist of several Raman active modes having very close frequencies.

There have been numerous investigations on $MgAl_2O_4$, $CaAl_2O_4$ and their solid solutions with Raman spectroscopy (Kojitani et al., 2007; Kojitani et al., 2013; Ono et al., 2009). Yet, there is no detailed Raman spectroscopic study on Fe-free and Fe-bearing CF phase. As shown in Figure 7, Raman modes located between 680-900 cm^{-1} become stronger and sharper at higher pressures in both phases. At ambient conditions, the peak at 190 cm^{-1} of Fe-free CF phase can be attributed to the vibrations of the Na^+ ions, while this peak is not observed in the Fe-bearing sample (Fei et al., 2020; Kojitani et al., 2013). The vibrational modes at ~348 cm^{-1} and 331 cm^{-1} in Fe-free and Fe-bearing CF phase, respectively, can be assigned to A_g modes with translation of Al^{3+} (Kojitani et al., 2013). Mode frequencies at 374, 439, 460, 554 and 653 cm^{-1} in the Fe-free sample and at 386, 453, 474, 535 and 631 cm^{-1} of Fe-bearing sample can be attributed to the O–Si–O and Si–O–Si (or Al) bending, which are accordance with the $MgAl_2O_4$ and $CaAl_2O_4$ in CF structure (Kojitani et al., 2013). In the frequency range of 680-900 cm^{-1}, the most intense peaks at 729, 772 cm^{-1} (Fe-free CF), and 720, 799 cm^{-1} (Fe-bearing CF) are mainly caused by the vibrational modes related to the octahedral sites. It should be noted that peak broadenings in the frequency range of

294 400-660 cm^{-1} and 680-900 cm^{-1} is generally associated with structural disorder over
295 lattice sites, i.e., Si, Al and Fe disorder over the octahedral site in the CF structure
296 (Kojitani et al., 2013). Therefore, spectral deconvolution in the region between 680-
297 900 cm^{-1} produces 3 main peaks around 720, 799, 839 cm^{-1} and 729, 772, 818 cm^{-1}
298 assigned to the $(Al/Si)O_6$ octahedral sites in Fe-rich and Fe-free CF phase,
299 respectively (Figure S3). It was found that the bands appearing at the 680-900 cm^{-1}
300 region in Fe-bearing CF phase tended to be broader than the pure-CF, due to presence
301 of Fe^{3+} in the octahedral sites. On this basis, the Raman bands become far apart with
302 elevated pressure, indicating less disorder in the octahedral Fe environments (Figure
303 S3). Additionally, at higher frequencies, the appearance of the peaks at 944, 985, 1099
304 cm^{-1} and 908, 980, 1080 cm^{-1} in Fe-free and Fe-rich CF sample, respectively, are
305 probably caused by Si–O_{nb} (non-bridged oxygen), Si–O_{br} (bridged oxygen) bending
306 asymmetric and symmetric stretchings (Prencipe, 2012).

307 Mode Grüneisen parameters (γ_i) were calculated using $\gamma_i = (K_0/\nu_i)\,(d\nu_i/dP)_T$, where
308 ν_i is the wavenumber of the i^{th} mode and K_0 is the bulk modulus at room temperature
309 (Table S7). Here, we used the isothermal bulk modulus K_0 of 220(4) and 211(6) GPa
310 for Fe-free and Fe-bearing CF phase, respectively, which were obtained by the BM3
311 fit. The resulting mean pressure coefficient of the whole structure for pure CF-
312 $NaAlSiO_4$ of 1.61(7) cm^{-1}/GPa is slightly higher than 1.40(6) cm^{-1}/GPa found for Fe-
313 bearing sample. Correspondingly, the calculated mode Grüneisen parameters
314 determined in this study range from 0.31(2)-0.94(2) for the pure-CF, and 0.25(3)-
315 0.84(2) for the Fe-bearing CF phase, with average values from all the observed modes

316 of 0.58(1) and 0.54(2), respectively. As for the octahedral site vibrations in both
317 phases, the calculated γ values fall generally in the range of 0.57-0.84, which are
318 comparable with those experimental determined modes with AlO_6 octahedra for
319 $MgAl_2O_4$ in the CF-type structure (Kojitani et al., 2013). The mean pressure
320 coefficient of octahedral site-derived mode in Fe-bearing CF phase of 2.78(7)
321 cm^{-1}/GPa is larger than 2.17(6) cm^{-1}/GPa found in Fe-free sample, consistent with the
322 higher compressibility of the Fe-bearing phase relative to Fe-free CF phase. We
323 therefore conclude that the major difference in compressibility between the two
324 structures is related to the Al/Fe–O bonds in octahedral sites in particular along the *c*-
325 axis.

326 **Implications**

327 Generally, the structural compression mechanisms of the CF and NAL phases
328 can be compared with the structural shrinkage in K-hollandite. With increasing
329 pressure, a distortion of the $(Al,Si)O_6$ octahedral framework, which forms the tunnel
330 structure, contracts and leads to more compact tunnels. Since the ^{VIII}K-O bond in K-
331 hollandite is one of the most compressible bonds among the metal-oxygen pairs in
332 oxide minerals, KO_8 polyhedra are very compressible and can be compared to the
333 bulk modulus of NaO_8 in the CF phase (Mookherjee and Steinle-Neumann, 2009;
334 Zhang et al., 1993). Furthermore, in comparison to jadeite-$NaAlSi_2O_6$ (McCarthy et
335 al., 2008; Posner et al., 2014), the longer Na–O bonds and low degree of NaO_8
336 polyhedra distortion in the CF phase determined here at high pressures likely
337 contribute to its wide stability over lower mantle conditions.

Na-bearing majorite and Na-rich pyroxene (e.g., $NaAlSi_2O_6$ jadeite, $NaFe^{3+}Si_2O_6$ aegirine) have similar chemical compositions and have also considered as potential hosts for Na in the Earth's mantle (Bindi et al., 2011; Xu et al., 2017). Previous studies have indicated that aegirine remains in the monoclinic $C2/c$ structure up to 60 GPa, with the NaO_8 polyhedron likely controlling bulk compressibility (Xu et al., 2017). However, the incorporation of Fe^{3+} to Na-pyroxene significantly increases the bulk modulus as well as the transition pressure for the pyroxene to garnet transition (Xu et al., 2017; Matrosova et al., 2019). Although sodium is significantly enriched in continental crust compared with oceanic crust, Na is an important incompatible element in the mantle because it partitions strongly into the MORB-forming melts below the spreading ridges (Hofmann, 1988). Thus, subduction of MORB recycles Na into the mantle where it contributes to melting in the upper-mantle wedge but is also likely carried deeper into the mantle. The CF phase is regarded as the only Na-dominated stable phase in the lower mantle down to ~2700 km.

Considering the potentially significant volume proportion of CF and NAL phases in deeply-subduced MORB, the elastic properties of these minerals and their compositional solid solutions are important for estimates of density and velocity of MORB. In more recent studies, coupled substitutions of Al^{3+} and Mg^{2+} in the CF structure by Na^{+} and Si^{4+} has limited influence on its elastic constants, but slightly weakens the elastic wave anisotropy (Zhao et al., 2018; Wang et al., 2020). Further investigations of the crystal chemistry on the CF phase at the pressure and temperature relevant to the lower mantle conditions are necessary. Most importantly,

adopting the thermo-elastic parameters of the CF-structure end-member to estimate the thermo-elastic properties of complex aluminous solid solutions would improve our understanding of the role recycled oceanic crust plays in the global alkali cycle with implications for the long-term evolution and internal heating of the Earth's mantle.

Acknowledgements

This research was supported by the National Natural Science Foundation of China (grant no. 42202040 and 42172076) and the Fundamental Research Funds for the Central Universities (grant no. 590421013). SDJ Acknowledges support from the US National Science Foundation grant EAR-1853521. Work performed at GSECARS (Sector 13) of the Advanced photon Source (APS) is supported by the NSF EAR-1634415 and the Department of Energy (DOE) DE-FG02-94ER1446. The APS at Argonne National Laboratory is supported by the DOE, Office of Science, under Contract No. DE-AC02-06CH11357. Experiments at Sector 13-BM-C of the APS used the PX^2 facility, supported by GSECARS and COMPRES under NSF Cooperative Agreement EAR-1661511. Use of the COMPRES-GSECARS gas loading system was supported by COMPRES under NSF Cooperative Agreement EAR-1606856.

References

Andrault, D., Fiquet, G., Guyot, F., and Hanfland, M. (1998) Pressure-induced Landau-type transition in stishovite. Science, 282(5389), 720–724.

Angel, R.J., Alvaro, M., and Gonzalez-Platas, J. (2014) EosFit7c and a Fortran module (library) for equation of state calculations. Zeitschrift für Kristallographie-Crystalline Materials, 229(5), 405–419.

Baur, W.H. (1974) The geometry of polyhedral distortions. Predictive relationships for the phosphate group. Acta Crystallographica Section B: Structural Crystallography and Crystal Chemistry, 30(5), 1195–1215.

Bina, C., and Helffrich, G. (2014) Geophysical constraints on mantle composition, in Treatise on Geochemistry, edited by H. D. Holland and K. K. Turekian, pp. 41–65, Elsevier, Oxford.

Bindi, L., Dymshits, A.M., Bobrov, A.V., Litasov, K.D., Shatskiy, A.F., Ohtani, E., and Litvin, and Yu. A. (2011) Crystal chemistry of sodium in the Earth's interior: The structure of $Na_2MgSi_5O_{12}$ synthesized at 17.5 GPa and 1700 °C. American Mineralogist, 96, 447–450.

Cameron, M., Sueno, S., Prewitt, C.T, and Papike, J.J. (1973) High-temperature crystal chemistry of acmite, diopside, hedenbergite jadeite, spodumene and ureyite. American Mineralogist: Journal of Earth and Planetary Materials, 58(7-8), 594–618.

Dera, P., Zhuravlev, K., Prakapenka, V.B, Rivers, M.L, Finkelstein, G.J, Grubor-Urosevic, O., Tschauner, O., Clark, S.M., and Downs, R.T. (2013) High pressure single-crystal micro X-ray diffraction analysis with GSE_ADA/RSV software. High Pressure Research, 33, 466–484.

Dolomanov, O.V., Bourhis, L.J., Gildea, R.J., Howard, J.A., and Puschmann, H. (2009) OLEX2: A complete structure solution, refinement and analysis program. Journal of Applied Crystallography, 42, 339–341.

Dubrovinsky, L.S., Dubrovinskaia, N.A., Prokopenko, V.B., and Le Bihan, T. (2002) Equation of state and crystal structure of $NaAlSiO_4$ with calcium-ferrite type structure in the conditions of the lower mantle. High Pressure Research, 22, 495–499.

Fei, G., Song, J., Chen, X., and Liu, X. (2020) Discovery of pressure-induced monoclinic to monoclinic phase transition above 60 GPa in single crystal $NaAlSi_2O_6$ jadeite. Journal of Raman Spectroscopy, 51, 844–850.

Fei, Y.W., Ricolleau, A., Frank, M., Mibe, K., Shen, G.Y., and Prakapenka, V.B. (2007) Toward an internally consistent pressure scale. PNAS, 104, 9182–9186.

French, S.W, and Romanowicz, B.A. (2014) Whole-mantle radially anisotropic shear velocity structure from spectral-element waveform tomography. Geophysical Journal International, 198(3), 1303–1327.

Fujino, K., Nishio-Hamane, D., Seto, Y, Sata, N., Nagai, T., Shinmei, T., Irifune, T., Ishii, H., Hiraoka, N., Cai, Y.Q., and Tsuei, K. (2012) Spin transition of ferric iron in Al-bearing Mg–perovskite up to 200 GPa and its implication for the lower mantle. Earth and Planetary Science Letters, 317-318, 407–412.

Fukao, Y., and Obayashi, M. (2013) Subducted slabs stagnant above, penetrating through, and trapped below the 660 km discontinuity, Journal of Geophysical Research: Solid Earth, 118, 5920–5938.

Fujino, K., Nishio-Hamane, D., Seto, Y., Sata, N., Nagai, T., and Shinmei, T. (2012) Spin transition of ferric iron in al-bearing mg–perovskite up to 200 GPa and its implication for the lower mantle. Earth and Planetary Science Letters, 317-318, 407–412.

Funamori, N., Jeanloz, R., Nguyen, J.H., Kavner, A., Cadwell, W.A., Fujino, K., Miyajima, N., Shinmei, T., and Tomioka, N. (1998) High-pressure transformation in $MgAl_2O_4$. Journal of Geophysical Research, 103, 20813–20818.

Guignot, N., and Andrault, D. (2004) Equations of state of Na–K–Al host phases and implications for MORB density in the lower mantle. Physics of the Earth and Planetary Interiors, 143, 107–128.

Hofmann, A.W. (1988) Chemical differentiation of the Earth: the relationship between mantle, continental crust, and oceanic crust. Earth and Planetary Science Letters, 90(3), 297–314.

Imada, S., Hirose, K., and Ohishi. Y. (2011) Stabilities of NAL and Ca-ferrite-type phases on the join $NaAlSiO_4$-$MgAl_2O_4$ at high pressure. Physics and Chemistry of Minerals, 38(7), 557–560.

Imada, S., Hirose, K., Komabayashi, T., Suzuki, T., and Ohishi, Y. (2012) Compression of $Na_{0.4}Mg_{0.6}Al_{1.6}Si_{0.4}O_4$ NAL and Ca-ferrite-type phases. Physics and Chemistry of Minerals, 39(7), 525–530.

Irifune, T. (1987) An experimental investigation of the pyroxene-garnet transformation in a pyrolite composition and its bearing on the constitution of the mantle. Physics of the Earth and Planetary Interiors, 45(4), 324–336.

Irifune, T., Fujino, K., and Ohtani, E. (1991) A new high-pressure form of $MgAl_2O_4$. Nature, 349(6308), 409–411.

Irifune, T., and Ringwood, A.E. (1993) Phase transformations in subducted oceanic crust and buoyancy relationships at depths of 600–800 km in the mantle. Earth and Planetary Science Letters, 117(1-2), 101–110.

Irifune, T., Ringwood, A.E., and Hibberson, W.O. (1994) Subduction of continental crust and terrigenous and pelagic sediments: an experimental study. Earth and Planetary Science Letters, 126(4), 351–368.

Irifune, T., Naka, H., Sanehira, T., Inoue, T., and Funakoshi, K. (2002) In situ X-ray observations of phase transitions in $MgAl_2O_4$ spinel to 40 GPa using multianvil apparatus with sintered diamond anvils. Physics and Chemistry of Minerals, 29, 645–654.

Jenkins, J., Deuss, A., and Cottaar, S. (2017) Converted phases from sharp 1000 km depth mid-mantle heterogeneity beneath Western Europe. Earth and Planetary Science Letters, 459, 196–207.

Kawai, K., and Tsuchiya, T. (2012) Phase stability and elastic properties of the NAL and CF phases in the $NaMg_2Al_5SiO_{12}$ system from first principles. American Mineralogist, 97(2-3), 305–314.

Kawai, K., and Tsuchiya. T. (2013) First-principles study on the high-pressure phase transition and elasticity of KAlSi3O8 hollandite. American Mineralogist, 98(1), 207–218.

Kesson, S.E., Gerald, J.D.F., and Shelley, J.M.G. (1994) Mineral chemistry and density of subducted basaltic crust at lower-mantle pressures. Nature, 372(6508), 767–769.

Kojitani, H., Többens, D.M., and Akaogi, M. (2013) High-pressure Raman spectroscopy, vibrational mode calculation, and heat capacity calculation of calcium ferrite-type $MgAl_2O_4$ and $CaAl_2O_4$. American Mineralogist, 98(1), 197–206.

Liu, L. (1977) High pressure $NaAlSiO_4$: the first silicate calcium ferrite isotype. Geophysical Research Letters, 4(5), 183–186.

Litasov, K.D., and Ohtani, E. (2005) Phase relations in hydrous MORB at 18–28 GPa: implications for heterogeneity of the lower mantle. Physics of the Earth and Planetary Interiors, 150(4), 239–263.

Lobanov, S.S., Hsu, H., Lin, J.F., Yoshino, T., and Goncharov, A.F. (2017) Optical signatures of low spin Fe^{3+} in NAL at high pressure. Journal of Geophysical Research: Solid Earth, 122(5), 3565–3573.

Mao, H.K., Xu, J.A., and Bell, P.M. (1986) Calibration of the ruby pressure gauge to 800 kbar

under quasi-hydrostatic conditions. Journal of Geophysical Research: Solid Earth, 91(B5), 4673–4676.

Matrosova, E.A., Ismailova, L., Bobrov, A.V., Bykova, E., Bykov, M., Glazyrin, K., and Dubrovinsky, L. (2019) Compressibility of two Na-rich clinopyroxenes: A synchrotron single-crystal X-ray diffraction study. American Mineralogist: Journal of Earth and Planetary Materials, 104, 905–913.

McCarthy, A.C., Downs, R.T., and Thompson, R.M. (2008) Compressibility trends of the clinopyroxenes, and in-situ high-pressure single-crystal X-ray diffraction study of jadeite. American Mineralogist, 93(1), 198–209.

Mookherjee, M., and Steinle-Neumann, G. (2009) Detecting deeply subducted crust from the elasticity of hollandite. Earth and Planetary Science Letters, 288(3-4), 349–358.

Momma, K., and Izumi, F. (2008) VESTA: A three-dimensional visualization system for electronic and structural analysis. Journal of Applied Crystallography, 41, 653–658.

Novak, G.A, and Gibbs, G.V. (1971) The crystal chemistry of the silicate garnets. American Mineralogist, 56(5-6), 791–825.

Ono, S., Ohishi, Y., and Mibe, K. (2004) Phase transition of Ca-perovskite and stability of Al-bearing Mg-perovskite in the lower mantle. American Mineralogist, 89(10), 1480–1485.

Ono, S., Ohishi, Y., Isshiki, M., and Watanuki, T. (2005) In situ X-ray observations of phase assemblages in peridotite and basalt compositions at lower mantle conditions: Implications for density of subducted oceanic plate. Journal of Geophysical Research: Solid Earth, 110(B2).

Ono, S., Ito, E., and Katsura, T. (2001) Mineralogy of subducted basaltic crust (MORB) from 25 to 37 GPa, and chemical heterogeneity of the lower mantle. Earth and Planetary Science Letters, 190(1-2), 57–63.

Ono, A., Akaogi. M., Kojitani, H., Yamashita. K., and Kobayashi, M. (2009) High-pressure phase relations and thermodynamic properties of hexagonal aluminous phase and calcium-ferrite phase in the systems $NaAlSiO_4$–$MgAl_2O_4$ and $CaAl_2O_4$–$MgAl_2O_4$. Physics of the Earth and Planetary Interiors, 174(1-4), 39–49.

Posner, E.S., Dera, P., Downs, R.T., Lazarz, J.D., and Irmen, P. (2014) High-pressure single-crystal X-ray diffraction study of jadeite and kosmochlor. Physics and Chemistry of Minerals, 41(9), 695–707.

Prencipe, M. (2012) Simulation of vibrational spectra of crystals by ab initio calculations: an invaluable aid in the assignment and interpretation of the Raman signals. The case of jadeite ($NaAlSi_2O_6$). Journal of Raman Spectroscopy, 43(11), 1567–1569.

Reid, A.F., and Ringwood, A.E. (1969) Newly observed high pressure transformations in Mn_3O_4, $CaAl_2O_4$, and $ZrSiO_4$. Earth and Planetary Science Letters, 6(3), 205–208.

Ricolleau, A., Perrillat, J.P., Fiquet, G., Daniel, I., Matas, J., Addad, A., Menguy, N., Cardon, H., Mezouar, M., and Guignot, N. (2010) Phase relations and equation of state of a natural MORB: Implications for the density profile of subducted oceanic crust in the Earth's lower mantle. Journal of Geophysical Research: Solid Earth, 115(B8).

Ringwood, A.E., and Green, D.H. (1966) An experimental investigation of the gabbro-eclogite transformation and some geophysical implications. Tectonophysics, 3(5), 383–427.

Romanowicz, B., and Wenk, H.R. (2017) Anisotropy in the deep Earth. Physics of the Earth and Planetary Interiors, 269, 58–90.

Sueda, Y., Irifune, T., Sanehira, T., Yagi, T., Nishiyama, N., Kikegawa, T., and Funakoshi, K.I. (2009) Thermal equation of state of $CaFe_2O_4$-type $MgAl_2O_4$. Physics of the Earth and Planetary Interiors, 174(1-4), 78–85.

Sun, S.S., Nesbitt, R.W., and Sharaskin, A.Y. (1979) Geochemical characteristics of mid-ocean ridge basalts. Earth and Planetary Science Letters, 44(1), 119–138.

Wang, W., Xu, Y., Sun, D., Ni, S., Wentzcovitch, R., and Wu, Z. (2020) Velocity and density characteristics of subducted oceanic crust and the origin of lower-mantle heterogeneities. Nature communications, 11, 1–8.

Wentzcovitch, R.M., Ross, N.L., and Price, G.D. (1995) Ab initio study of $MgSiO_3$ and $CaSiO_3$ perovskites at lower-mantle pressures. Physics of the Earth and Planetary Interiors, 90(1-2), 101–112.

Wu, Y., Wu, X., Lin, J.F., McCammon, C.A., Xiao, Y., Chow, P., and Qin, S. (2016) Spin transition of ferric iron in the NAL phase: Implications for the seismic heterogeneities of subducted slabs in the lower mantle. Earth and Planetary Science Letters, 434, 91–100.

Wu, Y., Qin, F., Wu, X., Huang, H.J., McCammon, C.A., Yoshino, T., Zhai, S.M., Xiao, Y.M., and Prakapenka, V.B. (2017) Spin transition of ferric iron in the calcium-ferrite type aluminous phase. Journal of Geophysical Research: Solid Earth, 122(8), 5935–5944.

Xu, J., Zhang, D., Fan, D., Downs, R. T., Hu, Y., and Dera, P. K. (2017) Isosymmetric pressure-induced bonding increase changes compression behavior of clinopyroxenes across jadeite-aegirine solid solution in subduction zones. Journal of Geophysical Research: Solid Earth, 122, 142–157.

Yamada, H., Matsui, Y., and Ito, E. (1983) Crystal-chemical characterization of $NaAlSiO_4$ with the $CaFe_2O_4$ structure. Mineralogical Magazine, 47(343), 177–181.

Yoder Jr, H.S., and Tilley, C.E. (1962) Origin of basalt magmas: an experimental study of natural and synthetic rock systems. Journal of Petrology, 3(3), 342–532.

Zhang, D., Dera, P.K., Eng, P.J., Stubbs, J.E., Zhang, J.S., Prakapenka, V.B., and Rivers, M.L. (2017) High pressure single crystal diffraction at PX^ 2 JoVE (Journal of Visualized Experiments), (119), e54660.

Zhang, J.M., Ko, J., Hazen, R.M., and Prewitt, C.T. (1993) High-pressure crystal chemistry of $KAlSi_3O_8$ hollandite American Mineralogist, 78(5-6), 493–499.

Zhao, M., Zhou, H., Yin, K., Sun, Y., Liu, X., Xu, S., and Lu, X. (2018) Thermoelastic properties of aluminous phases in MORB from first-principle calculation: Implications for Earth's lower mantle. Journal of Geophysical Research: Solid Earth, 123(12), 10-583.

552 ## Figure captions

553 **Figure 1** The crystal structure of the CF phase, determined at 41.3 GPa. The grey polyhedra
554 corresponded to the A sites, occupied by Na^{+} or Fe^{2+}, and the smaller purple octahedra correspond
555 to the B sites, occupied by Al^{3+} and Si^{4+}.

556 **Figure 2** Normalized lattice parameters of Fe-free (filled circles) and Fe-bearing (open circles) CF
557 phases as a function of pressure at room temperature. Equations of state fits are shown by solid
558 lines for the Fe-free phase and dashed lines for the Fe-bearing CF phase.

559 **Figure 3** Pressure–volume data for the CF-phase (filled circles) and Fe-bearing CF phase (open
560 circles) from this study compared with other compositions from previous work (Guignot and
561 Andrault, 2004; Imada et al., 2012; Wu et al.,2017). Solid curves show the fitted BM3 equations
562 of state from this study.

563 **Figure 4** Pressure dependence of the mean bond lengths of the two distinct $(Al,Si)O_6$ octahedra
564 and the NaO_8 polyhedra in the pure CF phase.

565 **Figure 5** Pressure dependence of the polyhedral volumes for the pure CF phase.

566 **Figure 6** Pressure dependence of the distortion indices of the two distinct $(Al,Si)O_6$ octahedra and
567 NaO_8 polyhedra for the pure CF phase.

568 **Figure 7** Selected Raman spectra of Fe-free CF phase (A) and Fe-bearing CF phase (B) at various
569 pressures. Individual plots of deconvoluted Raman spectra at ambient conditions are also shown.

570

Figure 1

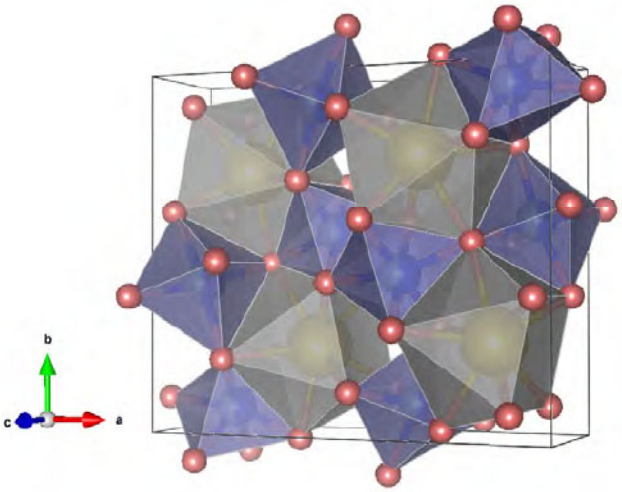

This is the peer-reviewed, final accepted version for American Mineralogist, published by the Mineralogical Society of America.
The published version is subject to change. Cite as Authors (Year) Title. American Mineralogist, in press.
DOI: https://doi.org/10.2138/am-2022-8432. http://www.minsocam.org/

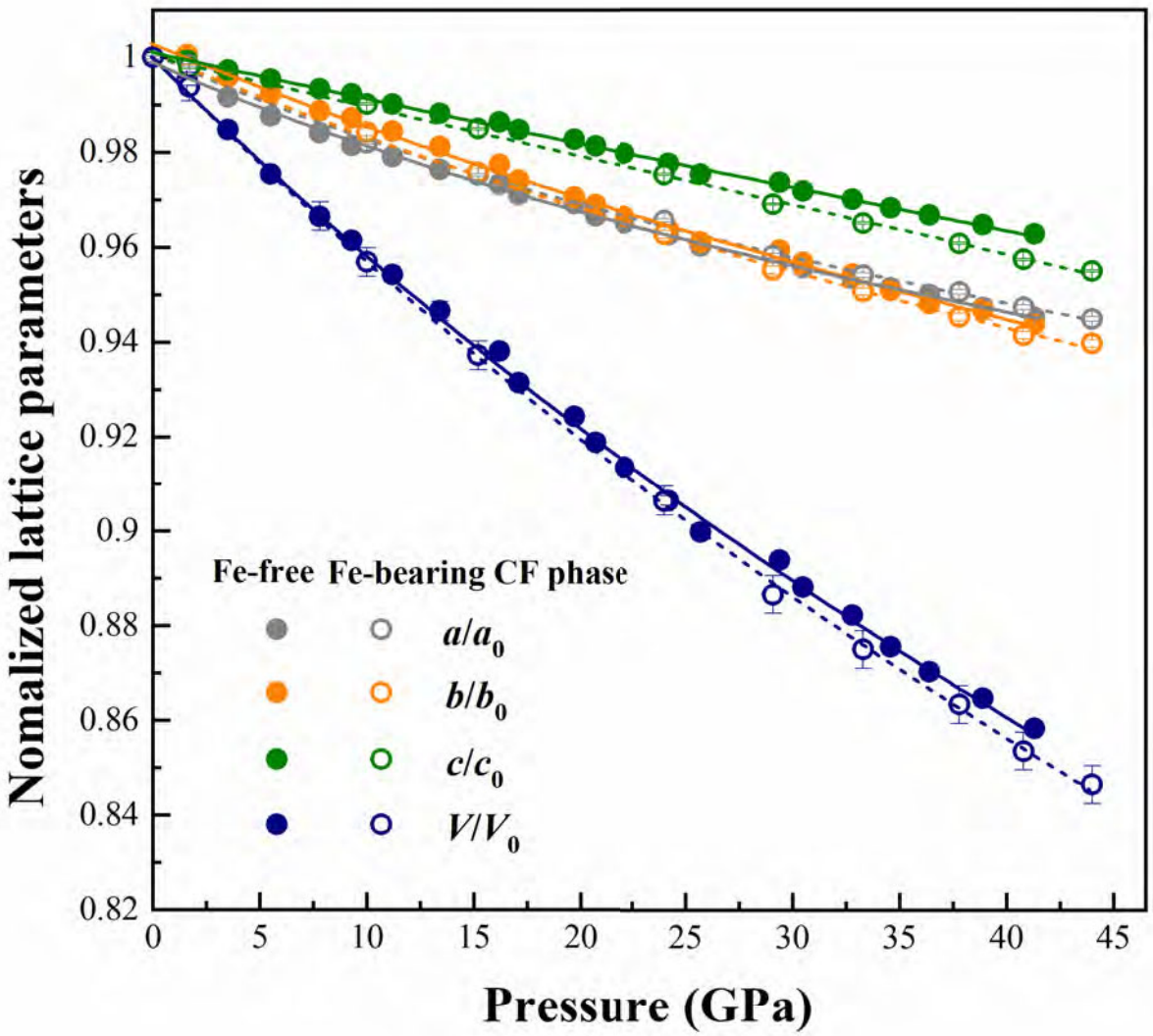

This is the peer-reviewed, final accepted version for American Mineralogist, published by the Mineralogical Society of America.
The published version is subject to change. Cite as Authors (Year) Title. American Mineralogist, in press.
DOI: https://doi.org/10.2138/am-2022-8432. http://www.minsocam.org/

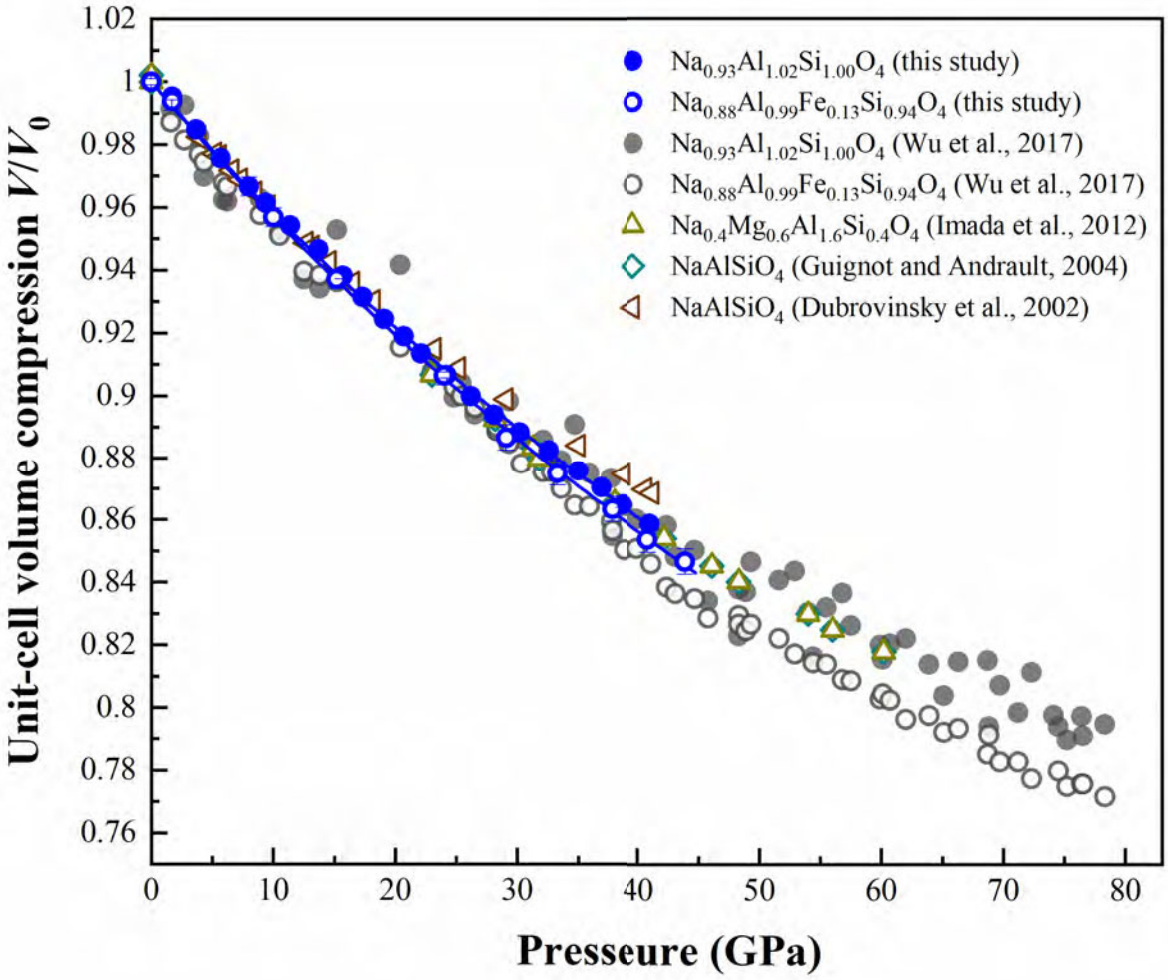

This is the peer-reviewed, final accepted version for American Mineralogist, published by the Mineralogical Society of America.
The published version is subject to change. Cite as Authors (Year) Title. American Mineralogist, in press.
DOI: https://doi.org/10.2138/am-2022-8432. http://www.minsocam.org/

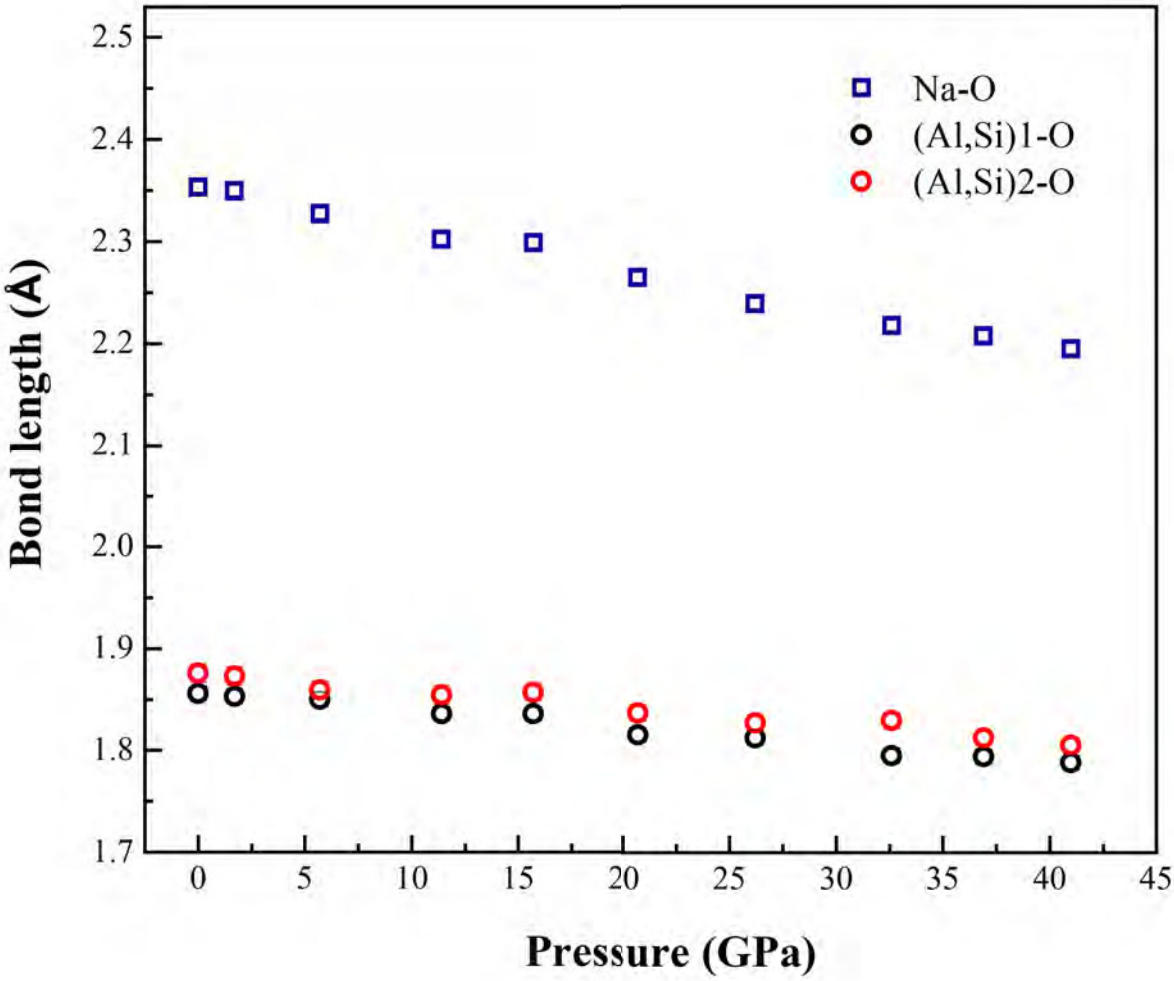

This is the peer-reviewed, final accepted version for American Mineralogist, published by the Mineralogical Society of America.
The published version is subject to change. Cite as Authors (Year) Title. American Mineralogist, in press.
DOI: https://doi.org/10.2138/am-2022-8432. http://www.minsocam.org/

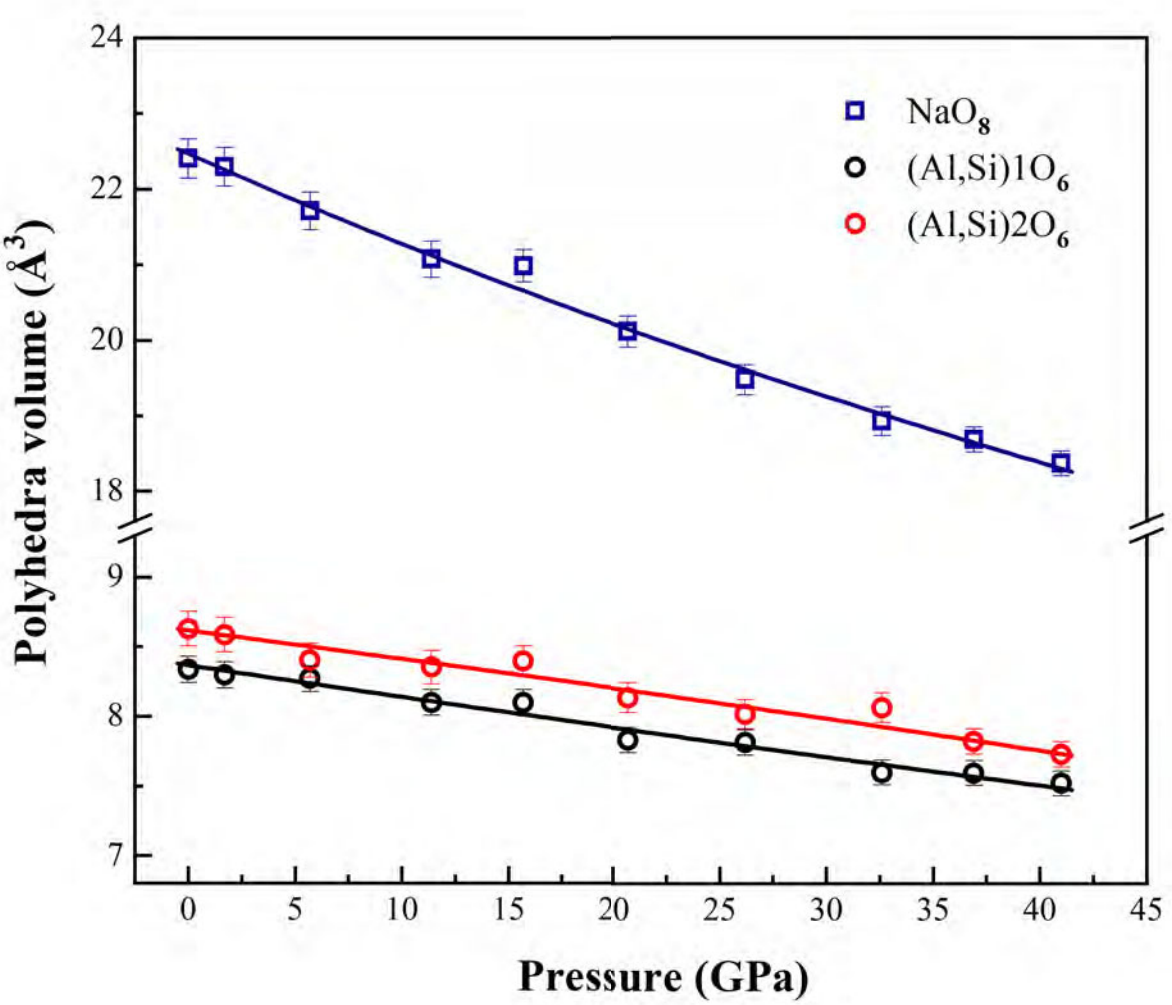

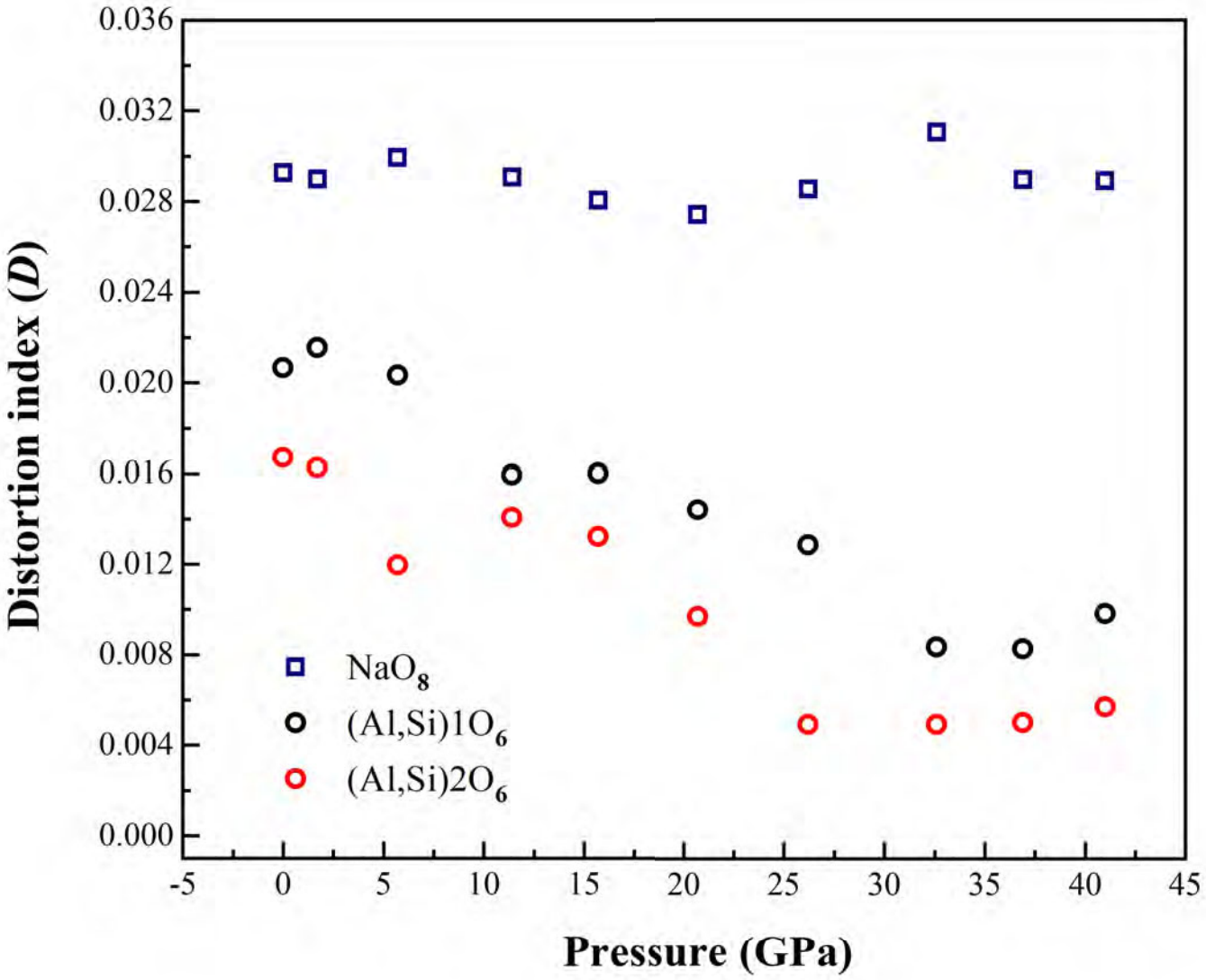

This is the peer-reviewed, final accepted version for American Mineralogist, published by the Mineralogical Society of America.
The published version is subject to change. Cite as Authors (Year) Title. American Mineralogist, in press.
DOI: https://doi.org/10.2138/am-2022-8432. http://www.minsocam.org/